Nanoscale

Accepted Manuscript

This article can be cited before page numbers have been issued, to do this please use: L. Xing and X. Tang, *Nanoscale*, 2026, DOI: 10.1039/D6NR00004E.

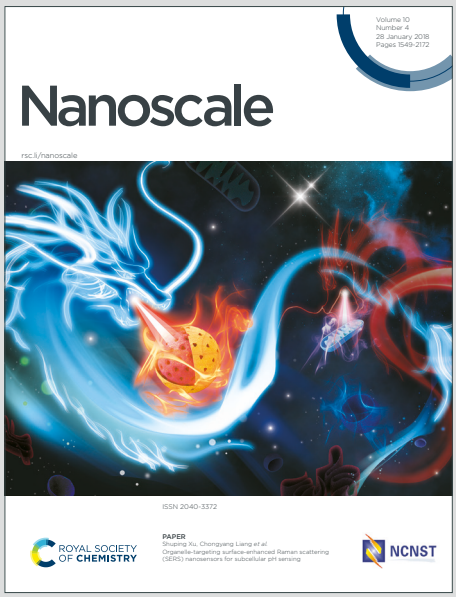

ROYAL SOCIETY OF CHEMISTRY

rsc.li/nanoscale

View Article Online
DOI: 10.1039/D6NR00004E

Journal Name

ARTICLE TYPE

Cite this: DOI: 00.0000/xxxxxxxxxx

Controlling particle dynamics in dead-end channels via boundary effects

Langqi Xing* and Xiaoyu Tang*†‡

Received Date
Accepted Date

DOI: 00.0000/xxxxxxxxxx

Controlled particle transport in confined geometries is crucial for advancements in fields ranging from targeted drug delivery to environmental remediation. Diffusiophoresis (DP) has been demonstrated to be a unique method to enhance efficiency and directionality of particle delivery. However, its counterpart, diffusioosmosis (DO) has received less attention in particle manipulation. Here, we systematically investigate the coupling between diffusiophoresis and diffusioosmosis to actively control particle transport in microfluidic dead-end pores. By exploiting solute concentration gradients and wall zeta potentials ζ_w, we achieve precise manipulation of colloidal particles without external power sources. Validated by experimental results, our established theoretical framework unveiled the intricate dependence of diffusioosmotic mobility (D_{DO}) on wall zeta potential and solute property and identified parameter ranges to flip the sign of D_{DO}. Furthermore, we introduced the concept of a critical reversal position y^*, the maximum transverse position where particles reverse direction within the dead-end pore, and proposed a scaling law and generated regime maps to characterize its dependence on critical parameters. These results provide essential insights for optimizing microfluidic designs for efficient particle transport. This work not only advances the fundamental understanding of electrokinetic phenomena in confined geometries, but also opens new avenues for designing passive, energy-efficient microfluidic systems for biomedical and environmental applications.

1 Introduction

Controlled particle transport in confined microscale environments underpins a wide range of technologies, including microfluidic analysis, porous-media remediation, and targeted delivery in complex geometries.[1–3] However, in dead-end or weakly connected microstructures, diffusion is slow and provides no intrinsic directionality, motivating passive strategies that convert solute–surface interactions into biased transport without imposed pressure or flow.[1,4,5]

Diffusiophoresis (DP) provides such a mechanism: colloids migrate relative to the surrounding fluid in response to solute concentration gradients. Its classical theory is well established for thin electrical double layers and electrolyte gradients.[4,6–10] Over the past decade, DP has been developed into a practical microfluidic transport modality for focusing, preconcentration, and separation, including configurations where gradients are generated and maintained in situ.[5,11–14] Importantly, DP is "motorless": it leverages ubiquitous gradients (salts, gases, metabolites) and can be implemented without electrodes or moving parts, which is attractive for low-power and field-deployable platforms.[14–18]

A particularly relevant and challenging class of geometries is the dead-end pore, a canonical element of porous networks and many biological microenvironments.[19–22] In dead-ends, gradients evolve strongly along the axial direction while the end wall enforces a no-flux constraint, producing a tight coupling between particle migration and any flow generated by interfacial mechanisms.[22–24] Prior studies have shown that electrolyte gradients can drive particles into dead-end pores and enable size- and charge-dependent penetration, highlighting dead-ends as a natural platform for gradient-driven delivery and selective access to clogged regions.[20,21] Recent work also emphasized that charge regulation—the concentration dependence of particle and wall zeta potentials—can qualitatively change predicted transport trends in dead-end configurations.[17,22,25]

Despite these advances, most dead-end DP studies treat the walls as electrokinetically uniform or emphasize the particle-scale DP mobility, while the wall-driven counterpart, diffusioosmosis (DO) receives comparatively less systematic treatment.[4,5] Yet, under the same solute gradients, DO can generate tangential slip along charged boundaries through mass conservation and pressure adjustment, inducing a bulk flow field that advects particles and can either reinforce or oppose DP.[26–33] This DP-DO interplay is especially significant in dead-end channels, where the global

* Department of Mechanical and Industrial Engineering, Northeastern University, MA 02115, United States.
† Department of Chemical Engineering, Northeastern University, MA 02115, United States.
‡ Email: x.tang@northeastern.edu

View Article Online
DOI: 10.1039/D6NR00004E

no-through-flow constraint promotes return-flow structures that can form near-wall reversal zones.[24,29,30] Moreover, practical devices often feature heterogeneous boundaries (different materials or coatings on opposing walls), which can break symmetry. However, a systematic framework connecting boundary zeta potentials to dead-end particle dynamics remains limited.[5,29]

Here, we address these gaps by systematically investigating particle transport in microfluidic dead-end channels under controlled electrolyte gradients while tuning boundary materials to vary wall zeta potential and its concentration dependence.[22,29] We develop and validate a coupled DP–DO framework that predicts the resulting bulk flow field and particle dynamics, and introduce a practical design metric—the critical reversal position y^*—that quantifies where particle reversal occurs across the channel width under symmetric and asymmetric boundaries.[22,23,30] Beyond providing mechanistic insight into boundary-controlled dead-end transport, these results offer materials-based guidelines for designing passive microfluidic architectures that selectively enhance entry, suppress clogging, or control access to otherwise occluded regions.[2,5,34,35] Dead-end geometries also appear in biomedical and tissue-mimetic microenvironments, which provides an additional motivation for understanding and controlling gradient-driven access in confined spaces.[36–38]

2 Theory

This section lays the theoretical background for this work, which stems from the coupling between the diffusiophoretic motion of the particle and the bulk flow in a dead-end channel induced by the diffusioosmotic fluid flow generated by different boundary materials. The solutions are discussed and compared with the experimental results in the result section 4.2.

2.1 Diffusiophoresis and diffusioosmosis

Diffusiophoresis (DP) describes the migration of colloidal particles driven by solute concentration gradients in the absence of external forcing. Following the classical electrokinetic framework for thin electrical double layers,[7,9,10,22,39] for a binary, monovalent electrolyte, the particle velocity can be written as

$$u_{DP} = D_{DP}\nabla \ln C, \tag{1}$$

where C is the local solute concentration and D_{DP} is the diffusiophoretic mobility,[4,5,17,40]

$$D_{DP} = \frac{\varepsilon}{2\eta}\left(\frac{k_B T}{Ze}\right)^2\left[2\beta\frac{Ze\zeta_p}{k_B T} + 8\ln\cosh\left(\frac{Ze\zeta_p}{4k_B T}\right)\right]. \tag{2}$$

Here, ζ_p is the particle zeta potential, ε is the permittivity of the medium, and η is the medium's viscosity, typically $0.001\,\mathrm{Pa\cdot s}$. The constants k_B, T, e, and Z represent the Boltzmann constant, absolute temperature (293 K), elementary charge, and solute valence ($Z_{Na^+} = -Z_{Cl^-} = 1$), respectively. The parameter $\beta = \frac{D_+ - D_-}{D_+ + D_-}$ captures the diffusivity difference between the cation and anion (e.g., for NaCl, $D_+ \approx 1.33\times10^{-9}\mathrm{m^2/s}$ and $D_- \approx 2.03\times10^{-9}\,\mathrm{m^2/s}$, gives $\beta \approx -0.21$).

Diffusioosmosis (DO) is the analogous interfacial response near a solid boundary: a solute concentration gradient generates a tangential slip flow along the wall.[22,29,41–43] In the thin double layer limit, the DO mobility has the same functional form as Eq. 2, but is in the opposite direction to DP and is evaluated using the wall zeta potential ζ_w,

$$D_{DO}(\zeta_w) = -D_{DP}(\zeta_p). \tag{3}$$

Eq. 2 naturally separates two contributions that are central to interpreting material- and solute-dependent trends of DP and DO. The first term in the bracket proportional to $\beta\zeta$ reflects the electrophoretic component arising from the local electric field generated by unequal ion diffusivities, while the second term with $\ln\cosh(\cdot)$ captures the chemiphoretic (osmotic) contribution associated with excess ion distributions in the double layer.[44,45] Together, these mechanisms set both the particle DP response and the wall-driven DO flow under the same imposed $\nabla\ln C$, enabling quantitative comparison across salts (via β and D) and materials (via ζ).

In the dead-end geometry of length L and width $2w$ with $w \ll L$ as shown in Fig. 1d, the solute concentration field follows the diffusion equation $\frac{\partial C}{\partial t} = D\frac{\partial^2 C}{\partial x^2}$,[20,23,24] with boundary conditions $C(0,t) = 0$ and $\partial C/\partial x(L,t) = 0$, and initial condition $C(x,0) = C_{\mathrm{solute}}$. The resulting series solution is

$$C(x,t) = \sum_{n=1}^{\infty}\left(\frac{4C_{\mathrm{solute}}}{(2n+1)\pi}\sin\left(\frac{(2n+1)\pi x}{2L}\right)e^{-D\left(\frac{(2n+1)\pi}{2L}\right)^2 t}\right), \tag{4}$$

where D is the ambipolar diffusivity $D = \frac{2D_+D_-}{D_+ + D_-}$ (for NaCl, $D \approx 1.61\times10^{-9}\,\mathrm{m^2/s}$). Concentration profiles used in calculations are summarized in the supporting information (*Analysis of NaCl Concentration Profile* and Fig. S3). Plugging Eqs. 2- 4 into Eq. 1 , the $u_{DP}(x,t)$ and $u_{DO}(x,t)$ can be calculated.

Note that throughout the work, we employ the thin-EDL ("slip") description for DP and DO, valid when $\lambda_D/w \ll 1$ (equivalently $\kappa w \gg 1$).[46–49] For the ionic strengths used here (sub-mM to $\mathcal{O}(10)$ mM), λ_D is on the order of nm to tens of nm, so $\lambda_D/w \sim 10^{-4}$–10^{-3}.

2.2 Bulk fluid velocity under different boundary conditions

We consider the two-dimensional dead-end channel in Fig. 1 with axial coordinate $x \in [0,L]$ (dead end at $x = L$) and transverse coordinate $y \in [-w,w]$. Since velocities in the system are small and the channel width is microscopic, inertia is negligible. A careful evaluation of the Reynolds number based on the half-width w,

$$\mathrm{Re}_w \equiv \frac{\rho U_0 w}{\eta}, \tag{5}$$

with $U_0 \sim 10^{-4}\ \mathrm{m\,s^{-1}}$ based on characteristic magnitude of the wall slip u_{DO}, $\rho \simeq 10^3\ \mathrm{kg\,m^{-3}}$, $\eta \simeq 10^{-3}\ \mathrm{Pa\,s}$, and $w \simeq 100\ \mu\mathrm{m}$ gives $\mathrm{Re}_w \sim 10^{-4} \ll 1$. the bulk flow satisfies the steady Stokes equations:[26–28,30]

$$-\nabla p + \eta\nabla^2\mathbf{u}_f = \mathbf{0}, \qquad \nabla\cdot\mathbf{u}_f = 0, \tag{6}$$

View Article Online
DOI: 10.1039/D6NR00004E

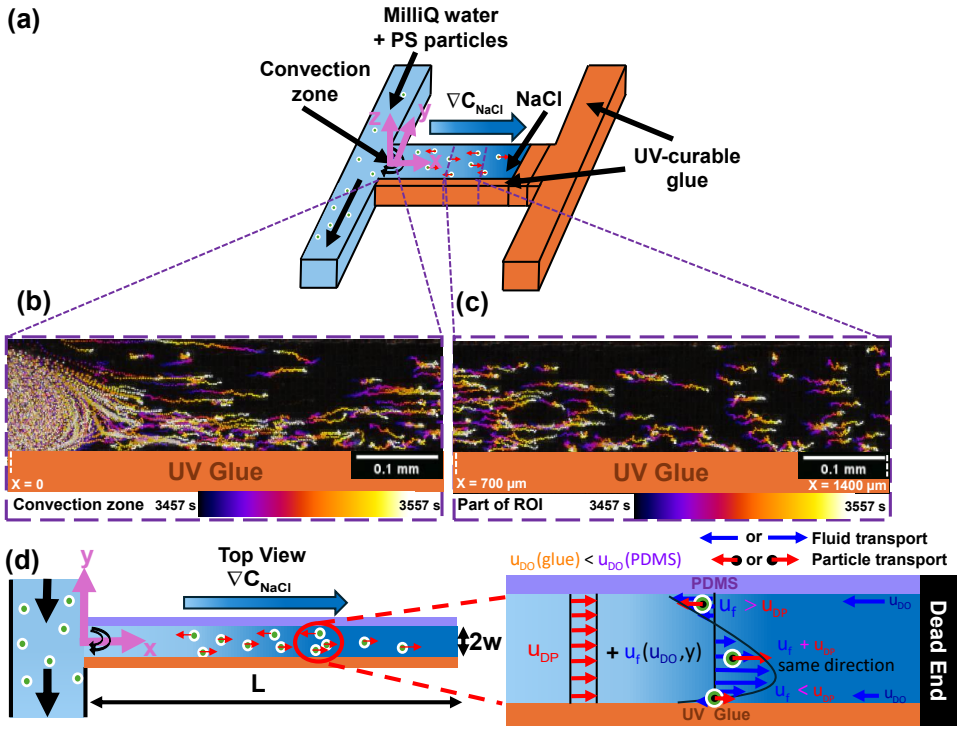

Fig. 1 (a) Schematic representation of the H-shaped dead-end microchannel system with asymmetric boundary materials. The channel geometry is shown with the lateral (x, y) and vertical (z) directions. In the asymmetric configuration, the channel boundaries are composed of polydimethylsiloxane (PDMS) (top wall) and UV glue (bottom wall). Polystyrene (PS) particles (green dots), suspended in MilliQ water, are introduced through the side channel and enter the dead-end channel pre-filled with NaCl solution, where their transport is governed by the coupled effects of diffusio-osmosis and diffusiophoresis. (b) Streakline image involves the convection zone (0 to 440 μm) at the inlet for t = 3457 to 3557 sec, where the particle location is color coded with time according to the color bar. It can be seen that particles move towards the dead-end in the bulk of the channel, while move out of the dead-end near the boundaries. (c) Streakline image of part of the region of interest (ROI) of length 700μm starting at 700μm from the inlet for t = 3457 to 3557 sec. (d) Schematic of the top view of the experimental region where particles are passed in the left channel and NaCl solution of 10mM concentration is pre-filled inside the dead-end channel, establishing a solute gradient towards the dead-end. The NaCl gradient induces a diffusioosmotic fluid flow u_{DO} near the wall pointing out of the dead-end and a diffusiophoretic particle motion u_{DP} pointing towards the dead-end. The DO flow near the wall further induced a bulk flow u_f due to mass conservation, as shown in blue in the blow-up schematic on the right. The particle motion is the superposition of u_{DP} and u_f. At the top PDMS surface, u_f wins, such that particle moves out of the dead-end pore. At the bottom glue surface, u_{DP} wins, such that particle moves towards the dead-end. In the bulk of the channel, u_{DP} and u_f synergistically move the particle towards the dead-end, as indicated by the pink arrow.

where $\mathbf{u}_f = (u_{f_x}, u_{f_y})$. The wall-driven diffusio-osmotic (DO) motion enters through slip boundary conditions at the walls,

$$u_{f_x}(x, \pm w, t) = u^{\pm}_{DO}(x,t), \tag{7}$$

where time dependence arises only through the slowly evolving solute field. The solute field evolves diffusively, so the DO slip generally depends on time through the evolving concentration gradient. We therefore write $u_{DO} = u_{DO}(x,t)$. The fluid responds quasi-instantaneously because the viscous diffusion time across the channel, $t_\nu \sim w^2/\nu$, is $\mathcal{O}(10^{-2}\,\mathrm{s})$ for $w \sim 100$ μm, far shorter than the solute diffusion times (minutes to hours). Consequently, at each time t the velocity field is well-approximated by a quasi-steady Stokes solution parameterized by t.

Under lubrication ($w \ll L$), the axial momentum balance reduces to[50–53]

$$\eta \frac{\partial^2 u_{f_x}}{\partial y^2} = \frac{\partial p}{\partial x}, \tag{8}$$

and the pressure is uniform across the width, $p = p(x,t)$. Integrating Eq. 8 twice and applying the slip conditions (Eq. 7) yields the general form

$$u_{f_x}(x,y,t) = \frac{1}{2\eta}\frac{\partial p}{\partial x}\left(y^2 - w^2\right) + \frac{u^{+}_{DO}(x,t) + u^{-}_{DO}(x,t)}{2} + \frac{u^{+}_{DO}(x,t) - u^{-}_{DO}(x,t)}{2}\frac{y}{w}. \tag{9}$$

The axial pressure gradient is determined by the dead-end constraint. Because the end wall is impermeable, the net cross-sectional flux must vanish:

$$Q(x,t) \equiv \int_{-w}^{w} u_{f_x}(x,y,t)\,dy = 0. \tag{10}$$

Substituting Eq. 9 into Eq. 10 gives

$$\frac{\partial p}{\partial x} = \frac{3\eta}{2w^2}\left(u^{+}_{DO}(x,t) + u^{-}_{DO}(x,t)\right). \tag{11}$$

Equations 9–11 together provide the bulk velocity field for time-dependent slips on the two walls.

View Article Online
DOI: 10.1039/D6NR00004E

2.2.1 Symmetric boundaries

The diffusio-osmotic velocity u_{DO} is identical at both walls, such that the boundary conditions for the bulk flow are $u_{f_x}(x,\pm w) = u_{DO}$. Solving Eq. 6 to Eq. 11 with these conditions yields the fluid velocity in the x-direction:

$$u_{f_x}(x,y,t) = \frac{u_{DO}(x,t)}{2}\left[3\left(\frac{y}{w}\right)^2 - 1\right]. \tag{12}$$

At the centerline ($y = 0$), the axial velocity simplifies to $u_{f_x} = -\frac{u_{DO}}{2}$, indicating a reversal in flow direction necessary to maintain zero net volumetric flux across any pore cross-section.

With mass conservation $\nabla \cdot \mathbf{u}_f = 0$, we derive the y-component of the fluid velocity:

$$u_{f_y}(x,y,t) = -\frac{\partial u_{DO}}{\partial x}\frac{y}{2}\left[\left(\frac{y}{w}\right)^2 - 1\right]. \tag{13}$$

Previous studies theoretically described the bulk flow motion in a 2-D scenario with same symmetric boundary conditions.[29,54] Their derived equations matched with our analytical results.

2.2.2 Asymmetric boundaries

For the case with asymmetric wall materials, the diffusio-osmotic velocities differ between the two walls, and the boundary conditions become $u_{f_x} = u_{DO1}$ at $y = -w$ and $u_{f_x} = u_{DO2}$ at $y = w$. Under these conditions, the fluid velocity in the x-direction is:

$$\begin{aligned} u_{f_x}(x,y,t) =& \frac{3y^2}{4w^2}\left(u_{DO1}(x,t) + u_{DO2}(x,t)\right) - \frac{3}{4}\left(u_{DO1}(x,t) + u_{DO2}(x,t)\right) \\ &+ \frac{y}{2w}\left(u_{DO2}(x,t) - u_{DO1}(x,t)\right) + \frac{u_{DO1}(x,t) + u_{DO2}(x,t)}{2}. \end{aligned} \tag{14}$$

Similarly, the y-component of the fluid velocity is given by:

$$\begin{aligned} u_{f_y}(x,y,t) =& -\frac{y^3}{4w^2}\left(\frac{\partial u_{DO1}}{\partial x} + \frac{\partial u_{DO2}}{\partial x}\right) + \frac{y^2}{4w}\left(\frac{\partial u_{DO1}}{\partial x} - \frac{\partial u_{DO2}}{\partial x}\right) \\ &+ \frac{y}{4}\left(\frac{\partial u_{DO1}}{\partial x} + \frac{\partial u_{DO2}}{\partial x}\right). \end{aligned} \tag{15}$$

At the centerline ($y = 0$), the axial velocity reduces to $u_{f_x} = -\frac{1}{4}\left(u_{DO1} + u_{DO2}\right)$, ensuring that the condition of zero net volumetric flux is satisfied.

As shown in Fig. 1d, different slip velocities generated at the top and bottom walls due to the asymmetric wall materials induced an asymmetric bulk velocity field in the dead-end channel, with the side of higher zeta potential (PDMS on the top in Fig. 1d) generating a higher u_{DO}, thus a larger zone with flow out of the dead-end. The fluid near the center of the channel flows into the dead-end due to mass conservation.

2.3 Particle velocity

The movement of particles within the system is the superposition of diffusiophoretic velocity u_{DP} due to the concentration gradient and bulk fluid velocity u_{f_x} induced by diffusioosmotic flow along the wall u_{DO}, which is typically in the opposite direction of u_{DP}. This relationship is encapsulated in the formula for the total velocity of particles u_{total} in the dead-end channel system:

$$u_{\mathrm{total}} = u_{\mathrm{DP}} + u_{f_x}, \tag{16}$$

Fig. 1d demonstrates the effect of the competition between u_{DP} and u_{f_x}. Near the center of the channel, u_{DP} and u_{f_x} act synergistically to move the particle towards the dead-end, while near the wall, u_{DP} and u_{f_x} points to opposite directions. If u_{f_x} wins, the particle is driven out of the dead-end, such as the PDMS case at the top wall. If u_{DP} wins or is comparable to u_{f_x}, particles move towards the dead-end or show no significant velocity.

3 Materials and methods

3.1 Microfluidic device preparation

Three-dimensional (3D) printed resin molds with an H-shaped channel structure were prepared to fabricate the microfluidic devices. The molds were printed using a standard translucent UV-curing resin (viscosity: 200–400 mPa · s). This patterned resin mold served as a template for replicating the H-shaped channels in polydimethylsiloxane (PDMS), enabling well-defined side and dead-end channel geometries.

PDMS devices were manufactured using the SYLGARD™ 184 silicone elastomer kit (Dow). The prepolymer and curing agent were mixed with a 10:1 weight ratio (viscosity of the base mixture: 3500 mPa · s), thoroughly stirred for at least 5 minutes to ensure uniformity, and then placed in a desiccator for a minimum of 1 hour to degas and remove trapped air bubbles. After degassing, the PDMS mixture was poured over the resin molds and subjected to a second degassing step to eliminate residual bubbles. The PDMS was then cured on a hot plate (Fisher Scientific Isotemp) at 75 °C for 10 hours , covered with an aluminum foil to maintain a consistent temperature during curing.

Once cured, patterned PDMS slabs were bonded onto glass slides. Bonding was achieved by activating surfaces using an ozone plasma cleaner (Novascan Technologies, Inc., United States) for 20 minutes to enhance adhesion between PDMS and glass. To tune boundary conditions beyond PDMS, UV-curable glue (NOA-81; Norland Products Inc., viscosity: 300 mPa · s) was patterned onto the channel walls to create either symmetric or asymmetric boundary materials. Specifically, depending on the desired configuration, UV glue was cured on (i) both opposing walls of the dead-end channel (symmetric glue–glue boundaries) or (ii) only one wall while the opposite wall remained PDMS (asymmetric PDMS–glue boundaries). Symmetric UV glue channels were made using PDMS molds fabricated by conventional soft lithography and microfluidic sticker techniques.[55–59]

Fig. 1 illustrates the H-shaped configuration employed in this study, featuring asymmetric boundaries. The side channel measures 600 μm in width, 4000 μm in length, and a fixed height of 15 μm, serving as the primary pathway for fluid flow. The dead-end channels have widths ranging from 180 to 280 μm and lengths between 3600 and 3800 μm. Channels with symmetric boundaries were fabricated with the same dimensional specifications to en-

View Article Online
DOI: 10.1039/D6NR00004E

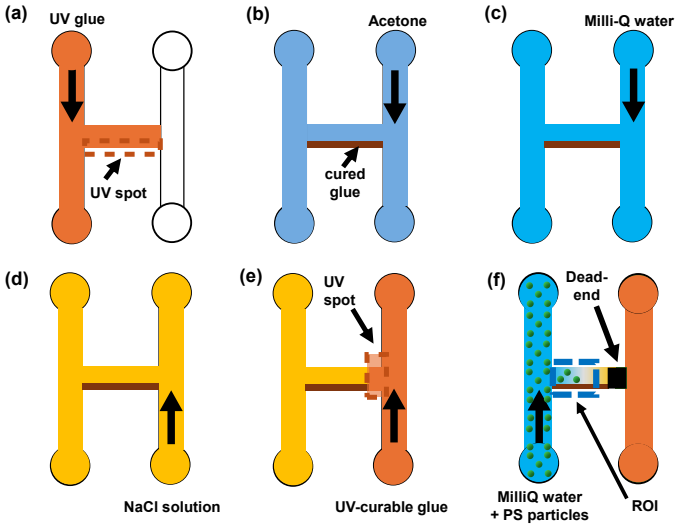

Fig. 2 Schematic illustrating the experimental procedures in an H-shape asymmetric microfluidic device with a dead-end pore. (a) UV glue is injected into the left channel, and UV light is exposed through a photomask slit at the bottom boundary of the middle channel to selectively cure the glue. (b) Uncured glue is removed by flushing acetone through the channel for over 1 hour to ensure complete dissolution. (c) The channel is rinsed by passing Milli-Q water for 8–12 hours to eliminate residual acetone and dissolved glue. (d) The channel is filled with NaCl solution. (e) The right-side channel is sealed by introducing UV glue and curing it with UV light at the junction with the middle channel. (f) The middle channel becomes an effective dead-end pore sealed with UV glue at the right end. For experiment, particle in MiliQ water is injected in the left side channel. The region of interest (ROI) for experimental observation is shown.

able direct comparison under identical geometry.

3.2 Experimental protocol

To create UV glue walls in the asymmetric boundary microfluidic devices, the device was first filled with NOA-81 using a syringe pump (Genie Touch, Kent Scientific, Connecticut), as illustrated in Fig. 2a. Ultraviolet (UV) light was directed through a rectangular photomask of controlled dimension placed at the microscope f-stop to polymerize the glue adjacent to the channel walls (Fig. 2a). With $5\times$ magnification (Nikon Plan Fluor, NA = 0.45), a 1-minute UV exposure cured a NOA-81 region approximately 40–60 μm in width and $\sim 300\,\mu$m in length. The cured feature length was primarily set by the photomask geometry, whereas the cured width depended on both the mask-defined geometry and the UV exposure time, which governs lateral curing beyond the nominal mask edge. By sequentially patterning seven partially overlapping exposures, a continuous glue wall spanning $\sim 3770\,\mu$m along the dead-end channel was generated, with an effective wall thickness of $\sim 50\,\mu$m (Fig. S7).

After wall formation, uncured glue was removed by flushing acetone ($\geq$ 99.5% purity; Sigma-Aldrich) through the device for over 1 hour to dissolve and remove residual NOA-81 (Fig. 2b). Milli-Q water was then flushed through the device for 8–12 hours to remove residual acetone and dissolved glue (Fig. 2c). For PDMS symmetric-boundary devices, experiments were conducted without the glue-wall patterning and solvent-cleaning procedures described above.

To initiate particle transport experiments, the entire device was filled with the desired NaCl solution (NaCl, 99% purity; Sigma-Aldrich) (Fig. 2d). UV glue was then introduced from one of the side channels and cured once it reached the UV spot at the entrance of the middle channel, creating the dead-end seal at the junction (Fig. 2e). Fluorescent carboxylated polystyrene particles (PS-COOH; Bangs Laboratories, Inc.; diameter $0.955 \pm 0.04\,\mu$m; stock concentration 1 wt%; absorption/emission 480/520 nm) were diluted in Milli-Q (MQ) water to a working concentration of 0.01% w/v to minimize particle–particle interactions and facilitate single-particle tracking. The suspension was vortexed for at least 5 minutes using a vortex mixer (OHAUS) and introduced into the opposite side channel, as shown in Fig. 2f.

Observations were performed using an inverted microscope (Zeiss Axio Observer, Carl Zeiss) equipped with a $5\times$ $f/0.25$ objective lens (depth of field 23 μm, *Zeiss LD Plan-Neofluar*) and a 20HE filter (Carl Zeiss). Image sequences were acquired for 2 hours at 1 frame per second (fps) using a monochromatic camera (ZEISS Axiocam 702, Carl Zeiss) with an image size of 1920×1216 pixels and a spatial calibration of 1.15 μm pixel^{-1}) using a $5\times$ objective with a $1\times$ adapter.

To verify that the observed transport is driven by diffusiophoresis rather than extraneous effects, control experiments were performed in the absence of a solute gradient as discussed in the supporting information section *Validation of Diffusiophoresis*. When particle suspension in MQ water was introduced into the side channel with the whole device filled with MQ water, no particles entered the dead-end channel (Fig. S6a), indicating negligible motion without a concentration gradient. By contrast, imposing a gradient by loading the dead-end channel with 10 mM NaCl while maintaining the particle suspension in MQ water led to clear particle migration into the dead-end channel (Fig. S6b). These results confirm that a solute concentration gradient is required to drive the observed transport, consistent with diffusiophoresis and diffusioosmosis reported in prior studies.[7,9,10,22,29,39,41–43]

General properties of the particle and wall materials are summarized in the supporting information Tab. S1 and Tab. S2.

3.3 Zeta potential characterization

Particle zeta potentials ζ_p were measured by electrophoretic light scattering using a Zetasizer Nano-ZS (Malvern Panalytical) with NaCl electrolytes spanning the ionic strengths used in the experiments from 0 to 10 *mM*, and are shown in Fig. S1 and Tab. 1.

To support the discussion of wall-driven electrokinetic effects, we compiled zeta potentials for the channel boundary materials. For PDMS, the surface zeta potential was taken from Akdeniz et al.[22] For UV glue, we experimentally measured the zeta potential by mechanically fragmenting cured NOA-81 into fine particulates and measuring their electrophoretic mobility using the Zetasizer under the same NaCl conditions as the flow experiments. While this particulate-based measurement does not reproduce a planar streaming-potential geometry, it provides a practical proxy for the sign and magnitude of the NOA-81 surface charge under the rel-

View Article Online
DOI: 10.1039/D6NR00004E

evant electrolyte conditions. The zeta potentials used for the boundary conditions are summarized in Tab. 1, with additional details provided in the supporting information (Fig. S2).

Table 1 Zeta potentials of particle and boundary materials.

Material	Method / source	ζ (mV)
Polystyrene Particle	Zetasizer on particulates	$-54\ to-44$
PDMS	Streaming potential[22]	$-106\ to-56$
UV Glue	Zetasizer on particulates	$-32\ to-18$

3.4 Quantitative measurements of particle velocity

The time-lapsed images showing the trajectories of individual particles were processed using *ImageJ* with the time marked by the color bar on the side, as shown in Fig. 1b and c, and also in Fig. 3a, b and c.[60] Accurate trajectories of the particles are obtained with custom code using *MATLAB* (MathWorks) adapted from Weeks, et al.[61]

To understand the distribution of the local velocity both along and across the dead-end channel, the channel is segmented into boxes of 300 μm in length along x axis and 25 μm in height along y axis, while the particle velocity along x-axis u_x averaged in each box is plotted in Fig. 3d, e and f. Detailed experimental error sources for particle detection and calculation methods and the calculation of the error bars are discussed in the supporting information Section *Experimental Error Sources*.

In addition to characterizing particle transport in the x-direction, we quantified the transverse (y-component) particle velocities as shown in the supporting information section *Analysis of the Y-Component of Particle Velocity*. Fig.S5 shows the y-component velocities of particles at t = 3557 s starting from particles flowing in the side channel. Across the majority of the field of view, the transverse velocities remain close to zero, indicating negligible lateral migration and confirming that the motion in the dead-end channel is predominantly unidirectional.

4 Results

4.1 Experimental particle dynamics near different boundary materials

The influence of boundary conditions on the dynamics of particles in the dead-end channel is investigated with three distinct boundary material conditions: PDMS on both top and bottom (Fig. 3a and d), UV glue on both top and bottom (Fig. 3b and e), and PDMS on the top with UV glue on the bottom (Fig. 3c and f). Measurements were taken in the Region of Interest (ROI) starting from 440 μm from the entrance of the dead-end channel, to minimize the impact of the convection zone shown in Fig. 1, to about 2200 μm.

Distinctive particle behaviors of the axial velocity profile across the channel width are observed for different configurations of boundary materials. For the channel with PDMS on both sides, while particles move towards the dead-end near the centerline of the channel, significant outflow is observed near the boundaries, signified by the bell shaped profile across the zero velocity in Fig. 3d. On the contrary, the velocity profile is much flatter for the channel covered with UV glue on both sides with lower zeta potential ($-32\ to-18\ mV$). Most particles migrate towards the dead-end, and the particles near the boundary show no significant differences in velocity from those near the centerline. For the asymmetric boundary case with PDMS at the top and glue at the bottom, the velocity profile is asymmetric, with particles near the centerline and the glue boundary moving towards the dead-end while particles near the PDMS boundary move in the opposite direction. Across all cases, particle velocity varied from $-1\,\mu m/s$ to $1.5\,\mu m/s$, with a general decreasing trend as the particles approached the dead-end pores due to a reduction in the solute concentration gradient.

The averaged velocity profiles in Fig. 3 are further supported by representative single-particle tracks reported in the Supporting Information (Figs. S8 and S9). For symmetric PDMS boundaries, the example trajectories show clear near-wall reversal/outflow consistent with strong wall-driven diffusio-osmotic backflow, whereas for symmetric NOA-81 boundaries the trajectories remain predominantly forward, consistent with weaker diffusio-osmotic advection. In the asymmetric case, the trajectories become side-dependent, with reversal signatures concentrated near the PDMS wall.

Qualitatively, the distinctive particle behaviors observed in the experiment highlight the critical role of the zeta potential of the boundary material in modulating particle dynamics in dead-end channels. The particle migration velocity is the superposition of the local fluid velocity and the diffusiophoretic velocity (Eq. 13). When the zeta potential of the wall is large, as in the PDMS case with ($-106\ to-56\ mV$), the induced diffusio-osmotic flow is significant and can win the competition with diffusiophoretic velocity, driving the particles out of the dead-end channel, as shown in Fig. 3a. On the other hand, diffusio-osmotic flow is weak near a wall with low zeta potential, as shown in the glue case ($-32\ to-18\ mV$), such that diffusiophoresis dominates leading to particle migration towards the dead-end.

Note that particles become sparse near the dead-end pore, which leads to insufficient tracking and therefore missing velocity data in those regions. This depletion is expected from a combination of transport and measurement effects: as particles progress deeper into the dead-end, the solute concentration gradient decreases, reducing both diffusiophoresis and any boundary-driven diffusio-osmotic advection, so fewer particles continue to advance into the terminal dead-end region. In addition, at lower local ionic strength, the electrostatic double layer thickens, which can increase the effective particle–wall repulsion and suppress near-wall occupancy. Consequently, particles tend to remain away from the channel wall.

4.2 Influence of boundary zeta potential on particle dynamics: Theoretical insights and experimental validation

Quantitative understanding of the effect of the boundary zeta potential on the particle dynamics in the dead-end channel is provided by comparing the results from the theoretical calculation based on section 2 with the experimental results discussed above, as shown in Fig. 4. The dots are x-velocities of particles extracted

View Article Online
DOI: 10.1039/D6NR00004E

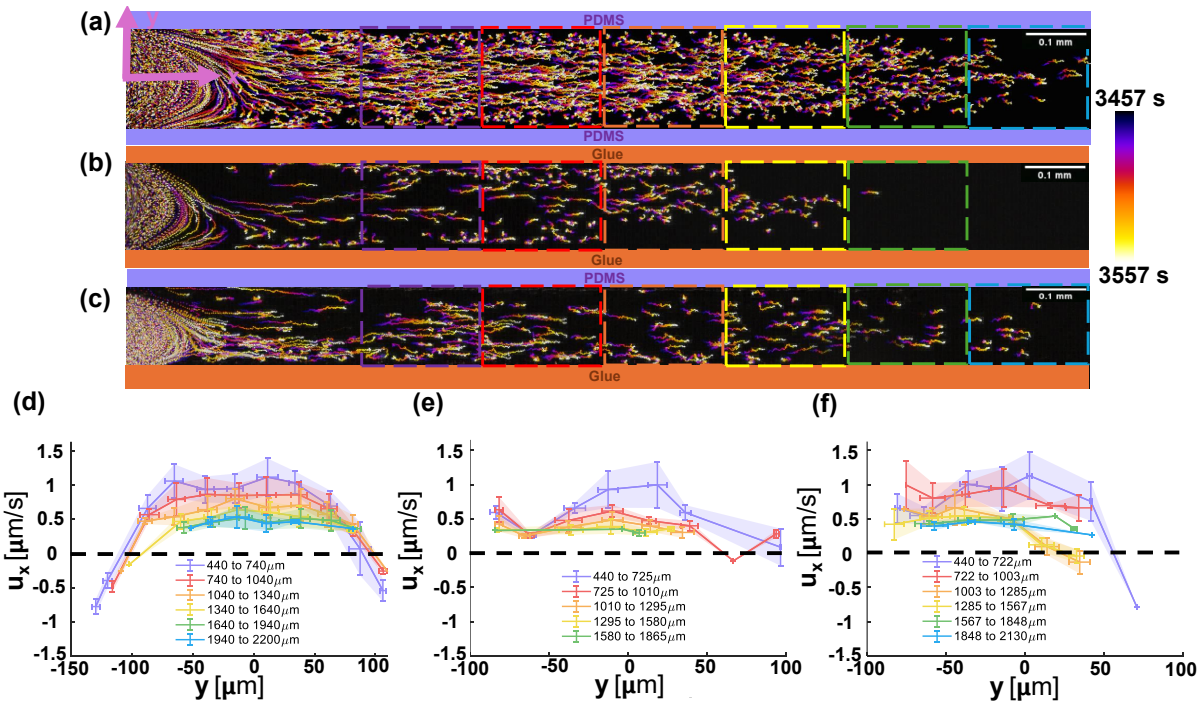

Fig. 3 Dynamics of particles with different boundary materials in the dead-end channel with a concentration gradient of $10mM$ NaCl pointing from left to right from t = 3457 to 3557 sec since the particle injection to the side channel. The particle x-velocity (u_x) is averaged within each y interval of 25μm. The color dashed boxes covered in the time-lapsed images corresponds to the same color legends in the particle velocity profiles from x $= \sim 440\mu$m to $\sim 2000\mu$m in the ROI to avoid the convection zone. Particle trajectory time-lapsed plot (a) and particle x-velocity profile (d) with both PDMS boundaries. Particle trajectory time-lapsed plot (b) and particle x-velocity profile (e) with both UV glue boundaries. Particle trajectory time-lapsed plot (c) and particle x-velocity profile (f) with asymmetric boundaries of top PDMS boundary and bottom UV glue boundary. Particle locations in (a-c) is color-coded in time as shown in the color bar on the right. Black dash lines in (d-f) denote where $u_x = 0$.

from experimental data, while the theoretical prediction of the particle velocities are shown with the shaded area. Both share the same color map for the velocity magnitude. Good agreement between the experimental results and the theoretical prediction is evident, showcasing the predictive power of our models.

Furthermore, the influence of boundary materials on particle dynamics is significant. Fig. 4a illustrates that particles near the PDMS boundaries within about 40μm, experience enhanced bulk fluid flow sufficient for egress from the dead-end pore. In contrast, Fig. 4b shows that for symmetrical glue boundaries, the bulk flow is considerably weaker, affecting particle movement minimally. As a result, particles are not transported out of the dead-end pore. Asymmetric boundary conditions further complicate particle dynamics, as shown in Fig. 4c, where particles exhibit different turning behaviors depending on their proximity to either PDMS or UV glue boundaries, which is consistent with our theoretical predictions.

Asymmetric boundary coatings not only modify the extent of reversal, but also break lateral transport symmetry and thereby introduce directional bias. These features enable one-sided protection, biased delivery, and passive steering in confined geometries, consistent with the broader concept of biomimetic anisotropy.[62] Such asymmetry could also support selective routing or separation when combined with particle properties such as shape, deformability, or surface chemistry.[63] More generally, patterned surface-charge studies show that boundary heterogeneity can generate structured microflows and recirculation without solid obstacles,[64,65] suggesting a practical route toward directional transport control through chemically patterned walls. In the next section, we provide a theoretical framework to predict and control the critical parameters to control particle transport which can serve as guidance for practical applications.

5 Discussion

5.1 Experimental parameters affecting the critical reversal location y^*

A central practical question in particle transport in dead-end pores is whether particles are retained inside the pore or expelled back into the main channel. We quantify this behavior using the critical reversal position y^*, which acts as a cross-stream separatrix: particles on one side of y^* are transported into the dead end, whereas particles on the other side are driven back toward the entrance. Thus, y^* directly measures the extent of the reversal (protection) zone across the channel width.

Because particle residence, trapping, and pore clearing are governed by this separatrix, y^* provides a direct design metric for applications that aim to either promote penetration into dead-end regions or mitigate fouling by biasing particles back out. In particular, a larger y^* indicates a wider near-wall region where wall-driven advection dominates, enabling more effective "push-back" toward the entrance and limiting deep particle intrusion, whereas a smaller y^* favors deeper entry and longer residence.

View Article Online
DOI: 10.1039/D6NR00004E

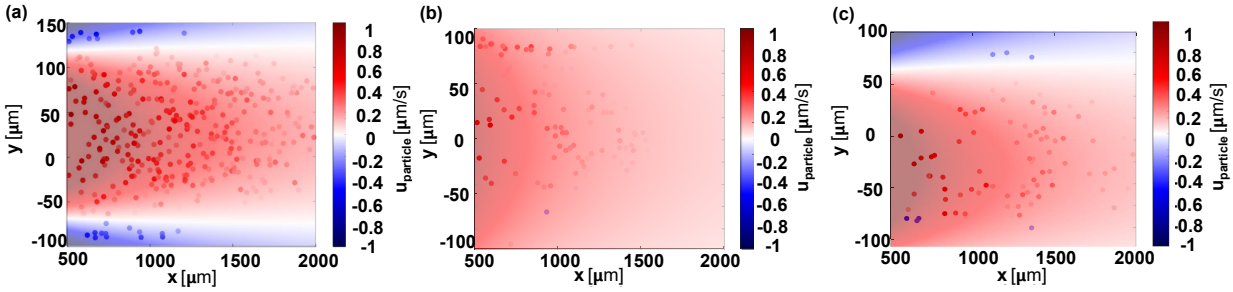

Fig. 4 Comparison of particle total velocity between experimental results and theory with different boundary materials: (a) symmetric boundaries with both PDMS, (b) symmetric boundaries with both UV glue, (c) asymmetric boundaries with top PDMS and bottom UV glue. The region shown is within the ROI in the dead-end channel and the time is from 3457 to 3557 sec. The dead-end channel is pre-filled with $10mM$ NaCl and water is flowing in the left side channel. The color dots represent experimental data, while the shaded color areas represent theoretical prediction. The color bar shows total particle velocities along x direction from negative (blue) to positive (red) values.

This balance is relevant to several confined transport settings.

In lab-on-a-chip diagnostic devices, dead-end grooves are often used as sensing or capture regions but are vulnerable to clogging; here, a controlled reversal region induced by boundary materials could allow target particles to enter while near-wall reverse motion helps sweep non-target debris back toward the main channel, reducing fouling and preserving sensor accessibility.[66–69] This interpretation is consistent with prior demonstrations of rapid and reversible accumulation of colloidal particles in dead-end microgrooved channels under salt gradients, as well as later work showing enhanced accumulation in microgrooved channels under steady electrolyte flows.[70,71] Related microfluidic studies have further shown solute-driven manipulation, preconcentration, sorting, and characterization of colloidal beads and liposomes, supporting the broader relevance of such transport control for bioanalytical cargo in confined microfluidic systems.[72] Designed boundary coatings enable an additional method to achieve precise control of particle transport without active switching of solute gradients.

In biomedical transport, especially in low-flow microvascular segments where particle–endothelium interactions are favored, a tunable y^* could help regulate particle interaction with endothelial boundaries and support localized delivery near vessel walls.[73,74] In porous environmental or subsurface systems, including remediation and oil recovery, the same mechanism could enable reversible transport of agents into and out of hidden or dead-end pores, where conventional advective flushing is ineffective.[75,76] More broadly, similar principles may be useful in confined manufacturing geometries such as high-aspect-ratio holes, blind cavities, or vias in semiconductor processing, where material delivery and redistribution inside restricted features must be controlled precisely.[77] From this perspective, y^* is not only a transport descriptor, but also a practical engineering metric for designing anti-fouling, boundary-targeted delivery, reversible extraction, and localized deposition in confined geometries.

Figure 5a illustrates the definition of y^*: the shaded bands denote the transverse region of particle reversal for two boundary materials, and y^* is the maximum distance from the boundary at which reversal occurs. $y^*(x)$ (for a given axial position x) is determined from the balance in Eq. 17, where diffusiophoretic motion $u_{DP} = D_{DP}\nabla \ln C$ is opposed by the bulk flow u_{f_x} generated by diffusio-osmotic slip $u_{DO} = D_{DO}\nabla \ln C$,

$$u_{\mathrm{DP}} + u_{f_x}(y = y^*) = 0. \tag{17}$$

Larger y^* values indicate stronger DO-driven advection and a broader reversal zone, whereas $y^* \approx 0$ indicates little or no reversal across the channel cross-section. In the following subsections, we show how y^* can be tuned using experimentally accessible knobs—channel geometry, boundary material properties, and solute choice (Fig. 5)—and translate these trends into practical guidance for shifting y^* upward or downward depending on the desired outcome.

5.1.1 Relationship between channel width and y^*

In this subsection we specifically consider the symmetric-boundary case (hence identical ζ_w), for which the diffusio-osmosis induced flow across the channel width admits the quadratic form (Section 2.2.1):[29,54]

$$u_{f_x} = \frac{u_{\mathrm{DO}}}{2}\left[3\left(\frac{y}{w}\right)^2 - 1\right], \tag{18}$$

where u_{DO} is set by the local salt gradient at x and the wall zeta potential $\zeta_w(C)$. Combining Eq. 17 and Eq. 18 yields a width-normalized scaling for the critical position,

$$\frac{y^*(x)}{w} \sim \left(\frac{\zeta_p(C)}{6\,\zeta_w(C)}\right)^{1/2}, \tag{19}$$

which is written in terms of the local zeta-potential ratio. Eq. 19 is therefore a scaling with respect to x through the salt concentration profile C: as the salt concentration varies along the dead-end channel, both ζ_p and ζ_w change with C, and their ratio sets the axial evolution of y^*/w.

Fig 5b illustrates this prediction for the PDMS–PDMS symmetric case, with same particle property and solute parameters as experiments. y^*/w decreases monotonically with x/L, indicating that the effective ratio ζ_p/ζ_w (evaluated at the local C) becomes smaller downstream, shifting the zero-velocity contour closer to the channel wall. Eq. 19 separates geometry from electrokinet-

View Article Online
DOI: 10.1039/D6NR00004E

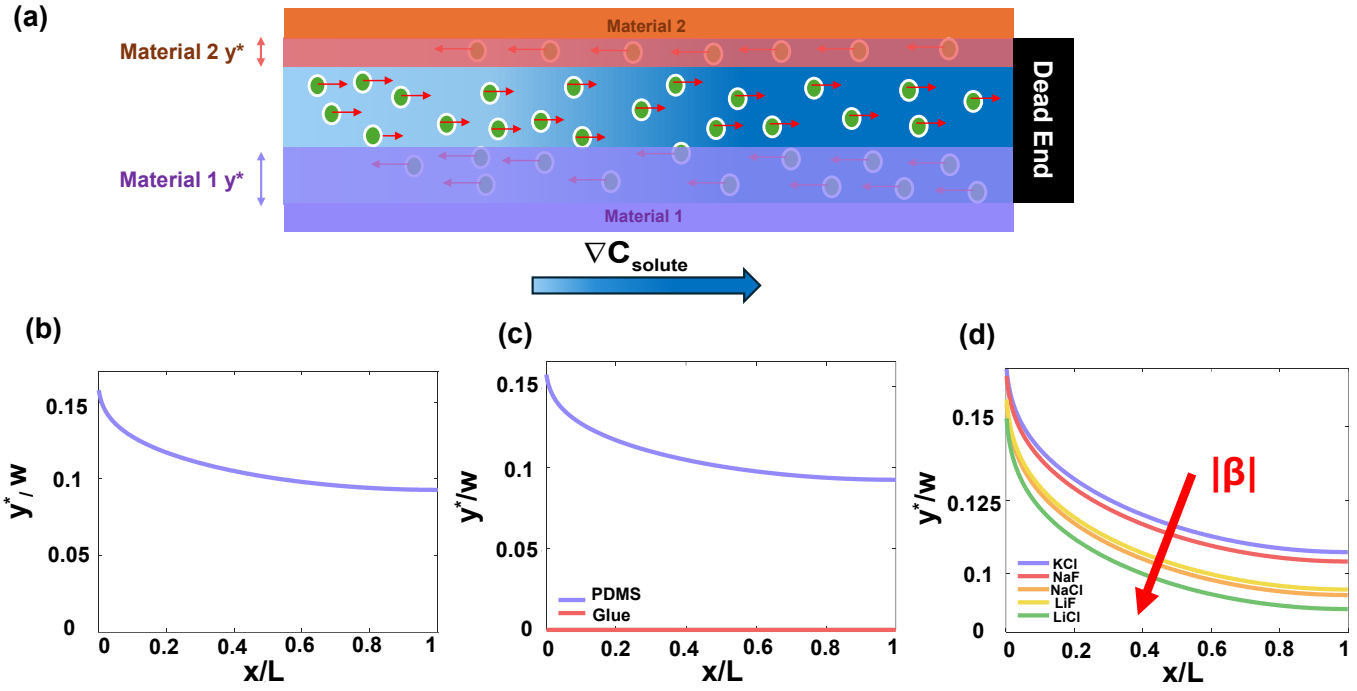

Fig. 5 Definition and dependence of the critical reversal position y^* on experimentally controlled parameters. (a) Schematic showing the definition of the critical reversal position y^*: the distance from the wall at which particle motion reverses. Material 1 on the bottom has a higher y^* than material 2 on the top, such that more particles move out of the dead-end pore near the bottom wall. (b) Scaling law of the critical reversal position y^* normalized by the channel width as a function of the location (x) in the channel normalized by the length of the channel (L). (c) Effect of wall material on the critical reversal position y^*. (d) Effect of types of solute on the critical reversal position y^*.

ics: for a fixed chemistry and concentration profile, increasing the channel width increases the absolute critical reversal position proportionally ($y^* \propto w$), whereas the normalized profile y^*/w is controlled by the zeta-potential ratio between particle and the wall and their salt dependence.

Although the above scaling is derived from a 2D width-wise description, our device geometry exhibits a strong separation of scales between height and width ($h/w = 0.075$). Consistent with this aspect ratio, the 3D analysis in the Supporting Information (*Effect of Channel Height on Critical Position* z^*; Fig. S4) shows that the critical reversal position in the vertical direction, z^*, remains confined very near the top/bottom walls (typically $\sim$ 1–2 μm, i.e., $z^*/h \leq 0.1$), whereas the corresponding lateral critical position, y^*, spans tens of microns (Fig. 5b, $y^*/w \approx 0.09$–0.16). Thus, z^* is significantly smaller than y^*, indicating that diffusio-osmotic flow effects associated with the channel height are weak compared with the dominant width-wise transport. This interpretation is further supported by the video observations (Videos S1–S7), where no appreciable return motion is observed in the mid-width region, and the reversal dynamics remain confined near the walls (y-direction). Together, this order-of-magnitude separation justifies neglecting height-driven 3D corrections under the conditions studied here and supports the 2D framework as an accurate reduced description of the observed particle dynamics.

Eqs. 17–19 provide a systematic recipe that can be translated to other systems: given (i) a predicted or measured concentration profile $C(x)$, and (ii) zeta-potential models $\zeta_p(C)$ and $\zeta_w(C)$ for the particle and the chosen wall material, one can directly estimate $y^*(x)$ and tune it. If the goal is a larger y^* (a broader region where particles can advance before reversal), the most direct handles are to increase the channel width w and/or increase the magnitude of the local ratio $|\zeta_p|/|\zeta_w|$ (e.g., more highly charged particles and/or less strongly charged walls, for like-signed ζ_p and ζ_w). Conversely, a smaller y^* can be achieved by reducing w and/or reducing $|\zeta_p|/|\zeta_w|$. Finally, if one seeks a $y^*(x)$ that varies weakly with x, then materials/conditions that reduce the salt-dependence of $\zeta_p(C)$ and $\zeta_w(C)$ (or that flatten $C(x)$ through geometry/operating protocol) will minimize axial drift in the critical contour.

5.1.2 Quantifying y^* for different material boundaries

Apart from the channel geometry as discussed above, the properties of the material also influence the critical reversal position y^*. To quantify y^* across various materials, we consider two symmetric material boundaries: PDMS and UV glue. The materials are chosen with distinctive zeta potential dependence on solute concentration.

For PDMS, we use the expression from Akdeniz et al.[22]:

$$\zeta_{\mathrm{PDMS}}(C) = -6.27 + 29.75 \log_{10}(C), \tag{20}$$

where ζ_w is in millivolts (mV) and C is the NaCl concentration in molar (M). For UV glue, we determine the concentration-dependent zeta potential by fitting experimental data with the logarithmic model proposed by Kirby et al.[78],

$$\zeta(C) = a + b \log_{10}(C), \tag{21}$$

View Article Online
DOI: 10.1039/D6NR00004E

which gives

$$\zeta_{\text{glue}}(C) = -13.76 + 3.19\log_{10}(C). \tag{22}$$

Fig. 5c compares the predicted critical reversal position $y^*(x)$ for symmetric PDMS and UV glue boundaries, with same channel dimension, particle property, and solute parameters as experiments. Two clear trends are evident. First, y^* decreases with increasing downstream distance x for PDMS and UV glue, indicating that the wall-driven advection that defines the separatrix weakens deeper in the dead-end channel. Second, the magnitude of y^* depends strongly on boundary material: PDMS yields a large y^* over the full x-range, and UV glue remains zero, implying a negligible exclusion region for UV glue under the same conditions.

These material-dependent trends follow from the fitted model $\zeta_w(C) = a + b\log_{10}(C)$, where a is the intercept at the reference point where $\log_{10}(C) = 0$. Because our experiments span the millimolar regime, the relevant comparison between PDMS and UV glue is evaluated over the concentration range generated in the channel (not a alone). Over this range, PDMS exhibits a larger magnitude of wall zeta potential than UV glue, which yields a larger $|D_{DO}|$ and hence stronger DO-driven wall slip (and associated near-wall backflow) for a fixed solute gradient. This increased backflow expands the portion of the cross-section advected toward the entrance and therefore increases the critical reversal position y^*, consistent with the larger y^* observed for PDMS.

The coefficient b governs how sensitively ζ_w responds to changes in local salt concentration along the channel. Because the concentration field varies with x, a larger $|b|$ amplifies the spatial variation of ζ_w, and hence amplifies the x-dependence of the diffusio-osmotic slip and the resulting $y^*(x)$, as seen in PDMS symmetric boundary case in Fig. 5c. Conversely, a smaller $|b|$ makes ζ_w less sensitive to $C(x)$, leading to a weaker variation of y^* with x.

5.1.3 Influence of solute type on y^*

The solute property affects the critical reversal position y^* primarily through the solute ion diffusivity difference β (Eq. 2). For a binary 1:1 electrolyte, unequal cation/anion diffusivities generate an electric field, derived from Nernst-Planck flux equation from Alessio et al.[29]:

$$\mathbf{E} \sim \frac{k_B T}{e}\beta\nabla\ln C, \tag{23}$$

which is the common physical origin of both diffusiophoresis (DP) of the particle and diffusioosmosis (DO) along charged channel walls. Consequently, the electrokinetic components of the two mobilities inherit the same β-dependence: $D_{\text{DP}} \propto \beta$ and $D_{\text{DO}} \propto \beta$ (Eq. 2), with prefactors set by the particle and wall electrostatic properties (e.g., ζ_p and ζ_w).

Figure 5d compares the theoretical predictions of y^* across several monovalent salts for the symmetric PDMS–PDMS case, using the same particle properties and solute conditions as in the experiments. The corresponding magnitudes of β follow

$$|\beta_{\text{LiCl}}| > |\beta_{\text{LiF}}| > |\beta_{\text{NaCl}}| > |\beta_{\text{NaF}}| > |\beta_{\text{KCl}}|. \tag{24}$$

As shown in Fig. 5d, salts with larger $|\beta|$ yield smaller y^*, whereas salts with smaller $|\beta|$ yield larger y^*.

Although D_{DP} and D_{DO} share the same β-scaling in their electrokinetic contributions, y^* is not controlled by that shared scaling alone; it is controlled by competition between (i) DP-driven particle drift relative to the local fluid and (ii) DO-driven wall slip that induces a bulk flow field (and associated pressure-driven return flow) that can entrain particles out of the dead-end. In practice, these two effects enter the particle kinematics with different prefactors and spatial structure: DP acts directly on the particle with a strength set by ζ_p, while DO acts through the walls with a strength set by both ζ_w and the channel geometry, and the resulting flow advects all particles occupying streamlines within the reversal region. Therefore, changing β amplifies both mechanisms, but the net outcome (larger vs. smaller y^*) is determined by which contribution dominates after accounting for their distinct prefactors and how the DO-generated fluid bulk flow redistributes streamlines across the cross-section, highlighting the complex dependence on different parameters of the problem.

The monotonic decrease of y^* with increasing $|\beta|$ in Fig. 5d indicates that, for the parameters used here, increasing $|\beta|$ strengthens the DP contribution sufficiently to shrink the range of initial transverse positions that can be swept out by DO-driven reversal. Conversely, selecting salts with smaller $|\beta|$ enlarges the reversal region and thus increases y^*. Therefore, solute choice provides a practical design lever: ions with more similar diffusivities favor stronger reversal and expulsion from the dead-end, whereas ions with more dissimilar diffusivities favor deeper penetration and reduced reversal.

5.2 Influence of salt property and boundary zeta potential on D_{DO}

The previous sections established the available experimental parameters to control y^*, now we will develop a theoretical framework to systematically predict the dependence of y^* on critical parameters. We first focus on D_{DO} which is critical in controlling y^*. This section will establish how D_{DO} is jointly controlled by the wall zeta potential ζ_{w} and the solute ion diffusivity difference β, based on Eqs. 2 and 3, and identify the parameter windows to achieve specific signs of D_{DO}.

As shown in Fig. 6a, for sufficiently large $|\beta|$ ($|\beta|$>0.43), D_{DO} varies nearly monotonically with ζ_{w}, providing a robust "design knob": changing the magnitude of surface charge produces a predictable change in the strength of diffusio-osmotic advection. In this regime, the sign of D_{DO} is well captured by the sign rule: $D_{DO} > 0$ when $\beta\,\zeta_{\text{w}} < 0$. Therefore, when $\beta\,\zeta_{\text{w}} < 0$, the induced flow is in the direction of $\nabla\ln C$, toward higher salt concentration; when $\beta\,\zeta_{\text{w}} > 0$, the flow reverses and points towards lower salt concentration.

The most practically important departure from monotonicity occurs when β is close to zero (cation and anion have similar diffusivities). In this limit, D_{DO} becomes small and non-monotonic

View Article Online
DOI: 10.1039/D6NR00004E

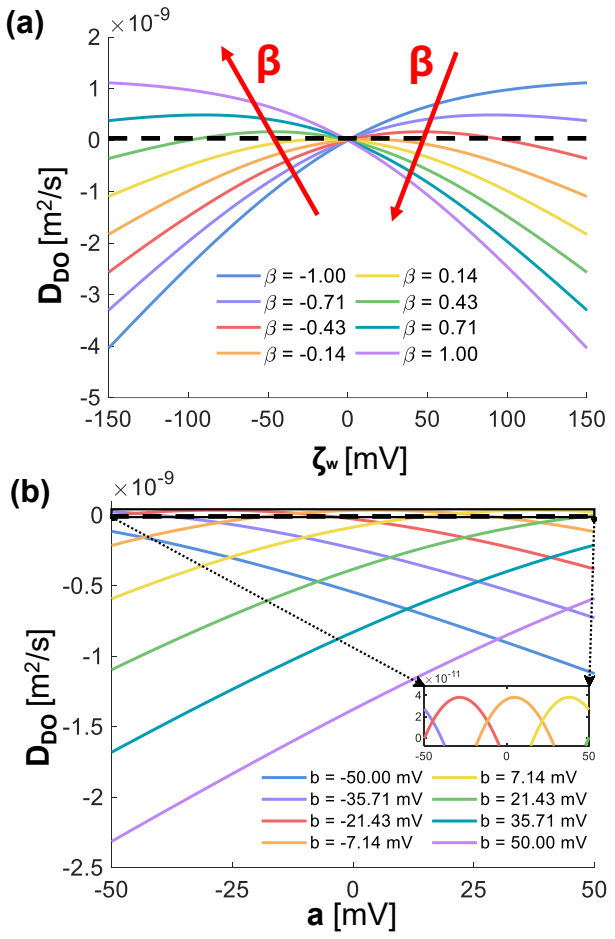

Fig. 6 Dependence of the diffusioosmotic mobility D_{DO} on surface zeta potential. (a) D_{DO} as a function of wall zeta potential ζ_w for different solute ion diffusivity difference β. (b) D_{DO} evaluated using Eq. 17 is plotted against parameter a for different parameter b. The solute concentration is taken at the channel midpoint ($\sim 1900\,\mu$m) based on the experiments. The inset highlights the narrow parameter window where D_{DO} approaches or exceeds zero. The black dashed line denotes $D_{DO} = 0$, separating regimes where diffusioosmotic slip (and the induced bulk flow) reverses direction.

in ζ_w, and only a limited range of ζ_w yields a sign change (crossing the dashed $D_{DO} = 0$ line). This "narrow switching window" is significant for two reasons: (i) it enables flow-direction control in otherwise impossible conditions with relatively small adjustments of surface chemistry (e.g., coating, plasma treatment, pH/ionic-strength conditioning that shifts ζ_w); (ii) it provides a route to fine balancing of advection against diffusiophoresis. Operating near $D_{DO} \approx 0$ suppresses background convection, which isolates diffusiophoretic contributions; conversely, deliberately moving across $D_{DO} = 0$ reverses the advective contribution, which can be used to promote entry versus expulsion from a dead-end, or to tune where a net-velocity cancellation occurs. For example, for a salt with $\beta = 0.14$ as shown in the yellow line in Fig. 6a, for a surface with negative ζ_w, a region of negative D_{DO} can be achieved, which is otherwise not possible within reasonable ζ_w for salts with $\beta > 0.43$.

Furthermore, the dependence of ζ_w on the solute concentration should also be considered (Eq. 17). Zeta potential measurements for carboxylated polystyrene particles, PDMS and UV glue confirm these trends, as detailed in Fig. S1 and Fig. S2. Using this model, D_{DO} is computed for NaCl ($\beta = -0.21$) gradient at the midpoint of the dead-end channel ($C = 3.4mM$) for different b values, as plotted against a in Fig. 6b. Rather than treating each curve individually, the key message is the narrowness of the region near $D_{DO} = 0$ (inset): D_{DO} becomes positive only within a restricted interval of a and b (b ≈ -35 mV to 20 mV with a ≈ -50 mV to 50 mV), while most (a,b) combinations yield $D_{DO} < 0$. This highlights that, under a fixed electrolyte (NaCl) and a fixed gradient, reversing the direction of diffusio-osmotic advection generally requires surfaces whose baseline zeta potential a lies in a relatively limited range.

The coefficient a sets the overall offset (baseline surface charge), while b controls how strongly the surface charge responds to changes in ionic strength along the gradient. Their distinct roles explain the trends in Fig. 6b: varying a moves the system toward or away from the sign-reversal window, whereas varying b reshapes the effective contribution of $\zeta_w(C)$ across the gradient. Consequently, b can either suppress or enhance $|D_{DO}|$ depending on whether the concentration-dependent shift in ζ_w pushes the surface potential toward (or away from) the narrow $D_{DO} \approx 0$ window. In practical terms, surfaces with similar ζ_w at a single reference concentration can still generate meaningfully different diffusio-osmotic advection if their b-values differ, because they experience different ζ_w profiles along the same salt gradient.

The theoretical net x-velocity fields (Fig. 4) are consistent with the experimental observations and help rationalize the material dependence of the reversal behavior. In particular, particles show no reversal near the UV-glue channels in contrast with the PDMS channels, consistent with the weaker wall-driven advection produced by the UV glue. Mechanistically, UV glue exhibits a smaller-magnitude wall zeta potential and a weaker concentration dependence (smaller $|b|$ in the charge-regulation model $\zeta(C) = a + b\log_{10}C$), which together reduce the magnitude and spatial variation of D_{DO}, and hence the effective slip $u_{DO} = D_{DO}\nabla \ln C$. As a result, the balance between diffusio-osmotic advection and particle diffusiophoresis is reached closer to the wall, producing no reversal.

Overall, Fig. 6 shows that both the magnitude and direction of diffusioosmotic advection are highly tunable through (i) solute choice via β, and (ii) surface charge level and regulation via ζ_w (or a,b). This provides a mechanistic basis for engineering particle transport in microfluidic dead-end channels: one can design conditions that robustly drive flow up- or down-gradient (large $|\beta|$, monotonic regime) or, alternatively, operate near the sign-flip window to achieve sensitive, switch-like control of background advection and the resulting particle-transport balance.

5.3 Regime maps of the critical reversal position y^*

While Fig. 6 identifies how D_{DO} is controlled, the more direct design metric is the critical reversal position y^*. The regime maps in Fig. 7 translate the electrolyte and surface dependencies of D_{DO} into this transport outcome. This connection is made explicit in

View Article Online
DOI: 10.1039/D6NR00004E

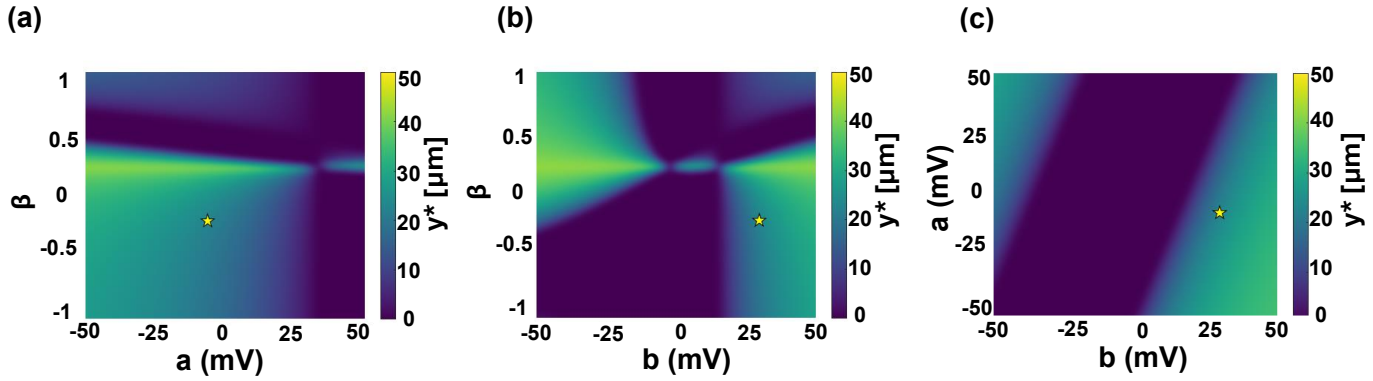

Fig. 7 Regime maps of the critical reversal position y^*. (a) Regime maps of y^* as a function of ion diffusivity difference β and wall charge-regulation parameter a in $\zeta_w(C) = a + b\log_{10}C$ (Eq. 21) with b fixed at $29.75mV$. (b) (β, b) with a fixed at $-6.27mV$. (c) (a, b) at fixed β at -0.21 (same as NaCl). The fixed a and b values are used from PDMS zeta potential values in Eq.S4 in the supporting information Section *Zeta Potential of Channel Boundary Materials (PDMS, NOA-81 glue, and glass*. The particle zeta potential value is used from Eq.S1 in the supporting information Section *Zeta Potential of PS-COOH Particle*. The position is at x = $1000\mu m$ and and the time is from 3457 to 3557 sec. Color bars indicate y^* (purple: $y^* \approx 0$, no/weak reversal; yellow: large y^*, strong reversal zone). The yellow star marks the nominal operating point with our experimental symmetric PDMS-PDMS boundary case used for comparison.

the (β, a) map with fixed b at $29.75mV$ (Fig. 7a), where we use a fixed b representative of the PDMS charge-regulation slope. For $\beta < 0$ (the NaCl case used in our experiments), increasing a shifts the wall potential ζ_w toward less negative (and eventually positive) values, producing a pronounced transition from a large-y^* regime at $a \approx -50$ mV to a small-y^* regime by $a \approx +50$ mV. This behavior is consistent with Fig. 6b: for the same fixed-b choice (between the representative curves around $b \approx 21.43$ mV and 35.71 mV), increasing a drives $|D_{DO}|$ toward smaller values (approaching the narrow window where $D_{DO} \approx 0$). Because u_{f_x} is generated by the DO slip and therefore scales with D_{DO}, a smaller $|D_{DO}|$ directly implies a weaker $|u_{f_x}|$; the bulk flow can no longer balance u_{DP} over an appreciable portion of the cross-section, so the cancellation point moves toward the wall and y^* decreases. In contrast, for $\beta > 0$ electrolytes, Fig. 6a indicates that D_{DO} remains close to zero over a wide, experimentally relevant wall-zeta potential range (e.g., $\zeta_w \sim -106$ to 56 mV in the plotted sweep). In that regime, the DO-driven bulk flow is intrinsically weak ($|u_{f_x}|$ small), so it cannot effectively compete with u_{DP}, and the resulting y^* stays small across much of the (β, a) space.

The remaining maps reinforce the same mechanistic link by showing how the charge-regulation slope b provides an additional lever to strengthen DO advection. In the (β, b) map with a fixed at $-6.27mV$ (Fig. 7b), larger $|b|$ increases how strongly ζ_w varies along the gradient through $\zeta_w(C) = a + b\log_{10}C$, which in turn increases $|D_{DO}|$ and strengthens $|u_{f_x}|$; consequently, the region where u_{f_x} can offset u_{DP} expands and y^* increases. This trend is consistent with Fig. 6b: at fixed a, increasing $|b|$ generally increases $|D_{DO}|$, directly amplifying the wall-driven contribution to the net transport balance. Finally, the (a, b) map with β fixed at -0.21 (Fig. 7c) collapses these ideas into a compact materials-design trade-off: combinations with larger $|a|$ and/or larger $|b|$ yield larger $|D_{DO}|$, hence larger $|u_{f_x}|$, and therefore larger y^*; conversely, (a, b) pairs that place the system near the narrow $D_{DO} \approx 0$ window produce weak advection and $y^* \approx 0$. Overall, Fig. 7 provides a direct design guide linking experimentally tunable parameters (β, a, b) to the reversal separatrix y^* through the intermediate control of D_{DO} and the resulting DO-driven bulk flow u_{f_x}, consistent with the material-dependent velocity-field trends discussed in Fig. 4.

From an engineering perspective, the y^* maps provide a direct route from measurable material/electrolyte properties to device-level transport behavior. A large y^* is desirable when one aims to create an extended reversal zone, for example to keep particles away from the wall, localize them at a controlled standoff distance, or enhance selective boundary-mediated redistribution. By contrast, $y^* \approx 0$ is preferable when more uniform forward penetration into the dead-end region is desired without appreciable turn-back. Accordingly, Fig. 7 can be interpreted as a practical design chart: one first selects the working electrolyte through β, and then chooses or modifies the boundary material through a and b to place the system in the region that yields the target particle transport behavior.

6 Conclusion and outlook

In this work, we have provided a comprehensive understanding of the effect of wall material on particle transport in microfluidic dead-end channels and unveiled the complex interplay between diffusiophoretic particle motion and bulk flow induced by diffusioosmotic slip flow and their dependence on system parameters. These understandings provide design guidelines for manipulating particle dynamics by tuning the wall zeta potential, solute type, and channel dimension.

We have provided a systematic understanding of the dependence of diffusioosmotic mobility D_{DO} on solute ion diffusivity difference β and wall zeta potential ζ_w. We showed that while the dependence is monotonic for the solute with $|\beta| > 0.43$, for solutes with $|\beta| < 0.43$, the nonmonotonic dependence leads to a narrow range of ζ_w for the sign reversal of D_{DO} , which provides a window to create particle motions that are otherwise challenging

View Article Online
DOI: 10.1039/D6NR00004E

to achieve. The parameters a, b in the dependence of ζ_w on the solute concentration C can also be utilized to fine tune the sign and magnitude of D_{DO}.

We introduced the concept of the critical reversal position y^*, a key parameter that delineates the maximum transverse location at which particles reverse direction within the pore. Based on this framework, we derived a scaling law for the dependence of y^* on the governing parameters and showed that larger y^* can be achieved using materials with higher wall zeta potentials ζ_w, such as PDMS, and solutes with larger diffusivity difference β.

Along with the relationships established for D_{DO}, these scaling results provide practical guidance for designing microfluidic systems for efficient particle manipulation. To extend this insight into a predictive design framework, we further constructed regime maps of y^* that reveal how the reversal zone depends on diffusivity difference β and wall charge-regulation parameters a and b, thereby identifying operating regimes that promote either stronger or weaker particle turn-back. Taken together, these results show that particle transport can be tailored through various selection of wall materials and solute gradients, enabling passive control without external energy input and advancing more sustainable microfluidic design.

Our work advances the understanding of electrokinetic transport in confined microscale geometries and offers practical guidance for the design of systems relevant to targeted drug delivery and environmental remediation. Future studies may extend these ideas to more complex fluidic networks, heterogeneous particle systems, and hybrid passive–active transport strategies to achieve greater control and efficiency. An especially promising direction is the use of patterned or dynamically tunable boundary coatings, which may exploit transport asymmetry to enable selective routing, localized mixing, and multifunctional microfluidic operation.

Author contributions

L. X. and X. T. designed the research. L. X. fabricated the devices and designed the experiments with input from X. T. L. X. performed experiments and analyzed the data. L. X. and X. T. discussed the results. L. X. and X. T. wrote the paper and revised the paper.

Conflicts of interest

There are no conflicts to declare.

Data availability

The data supporting this article, including the processed datasets, representative raw microscopy images, and analysis scripts, are provided in the Supplementary Information (SI).

Acknowledgements

L.X. is grateful to Boqian Yan for helpful discussions and a thorough reading of the manuscript.

Notes and references

1 T. M. Squires and S. R. Quake, *Reviews of Modern Physics*, 2005, **77**, 977–1026.
2 L. Bocquet and E. Charlaix, *Chemical Society Reviews*, 2010, **39**, 1073–1095.
3 R. Langer, *Science*, 1990, **249**, 1527–1533.
4 D. Velegol, A. Garg, R. Guha, A. Kar and M. Kumar, *Soft Matter*, 2016, **12**, 4686–4703.
5 S. Shim, *Chemical Reviews*, 2022, **122**, 6986–7009.
6 A. Monier, B. Byerley, J. Renaudeau, H. D. Ou-Yang, P. Lidon and J.-B. Salmon, *Langmuir*, 2025, **41**, 34554–34564.
7 B. Derjaguin, G. Sidorenkov, E. Zubashchenko and E. Kiseleva, *Kolloidn. Zh.*, 1947, **9**, 335–347.
8 B. Derjaguin, S. Dukhin and A. Korotkova, *Kolloid. Zh.*, 1961, **23**, 53–58.
9 J. L. Anderson, M. E. Lowell and D. C. Prieve, *Journal of Fluid Mechanics*, 1982, **117**, 107–121.
10 J. Anderson, *Annual Review of Fluid Mechanics*, 1989, **21**, 61–99.
11 N. Shi, R. Nery-Azevedo, A. I. Abdel-Fattah and T. M. Squires, *Physical Review Letters*, 2016, **117**, 258001.
12 J. S. Paustian, C. D. Angulo, R. Nery-Azevedo, N. Shi, A. I. Abdel-Fattah and T. M. Squires, *Langmuir*, 2015, **31**, 4402–4410.
13 R. Nery-Azevedo, A. Banerjee and T. M. Squires, *Langmuir*, 2017, **33**, 9694–9702.
14 S. Shin, O. Shardt, P. B. Warren and H. A. Stone, *Physical Review X*, 2017, **7**, 041050.
15 D. C. Prieve, S. M. Malone, A. S. Khair, R. F. Stout and M. Y. Kanj, *Proceedings of the National Academy of Sciences of the United States of America*, 2019, **116**, 18257–18262.
16 P. R. Shah, H. Tan, D. Taylor, X. Tang, N. Shi, A. Mashat, A. Abdel-Fattah and T. M. Squires, *Lab on a Chip*, 2022, **22**, 1980–1988.
17 A. Gupta, S. Shim and H. A. Stone, *Soft Matter*, 2020, **16**, 6975–6984.
18 S. Shim and H. A. Stone, *Proceedings of the National Academy of Sciences of the United States of America*, 2020, **117**, 25985–25990.
19 Y. Li, M. Alipour and A. A. Pahlavan, *arXiv preprint arXiv:2510.24938*, 2025.
20 S. Shin, J. T. Ault, P. B. Warren and H. A. Stone, *Proceedings of the National Academy of Sciences of the United States of America*, 2016, **113**, 257–261.
21 S. Battat, J. T. Ault, S. Shin, S. Khodaparast and H. A. Stone, *Soft Matter*, 2019, **15**, 3879–3885.
22 B. Akdeniz, J. A. Wood and R. G. H. Lammertink, *Langmuir*, 2023, **39**, 2322–2332.
23 J. T. Ault, P. B. Warren, S. Shin and H. A. Stone, *Soft Matter*, 2017, **13**, 9015–9023.
24 J. T. Ault, P. B. Warren, S. Shin and H. A. Stone, *Journal of Fluid Mechanics*, 2018, **854**, 420–448.
25 H. Tan, A. Banerjee, N. Shi, X. Tang, A. Abdel-Fattah and T. M. Squires, *Science Advances*, 2021, **7**, eabh0638.
26 A. Ajdari and L. Bocquet, *Physical Review Letters*, 2006, **96**, 186102.
27 H. J. Keh and H. C. Ma, *Langmuir*, 2005, **21**, 5461–5467.

View Article Online
DOI: 10.1039/D6NR00004E

28 S. Marbach and L. Bocquet, *Chemical Society Reviews*, 2019, **48**, 3102–3144.
29 B. M. Alessio, S. Shim, E. Mintah, A. Gupta and H. A. Stone, *Physical Review Fluids*, 2021, **6**, 054201.
30 B. M. Alessio, S. Shim, A. Gupta and H. A. Stone, *Journal of Fluid Mechanics*, 2022, **942**, A23.
31 S. Zhang and H. C. W. Chu, *Nanoscale*, 2024, **16**, 9367–9381.
32 S. Zhang and H. C. W. Chu, *Chemical Science*, 2024, **15**, 18476–18489.
33 H. Liu and A. A. Pahlavan, *Physical Review Letters*, 2025, **134**, 098201.
34 R. S. Sharma, W. Sarlin, L. Xing, C. Morize, P. Gondret and A. Sauret, *Physical Review Fluids*, 2024, **9**, 074301.
35 D.-H. Jeong, L. Xing, M. K. H. Lee, N. Vani and A. Sauret, *Journal of Colloid and Interface Science*, 2023, **650**, 407–415.
36 C. Bastiancich, G. Bastiat and F. Lagarce, *Drug discovery today*, 2018, **23**, 416–423.
37 P. E. Oberstein and K. P. Olive, *Therapeutic advances in gastroenterology*, 2013, **6**, 321–337.
38 A. Shergalis, A. Bankhead, U. Luesakul, N. Muangsin and N. Neamati, *Pharmacological reviews*, 2018, **70**, 412–445.
39 S. Dukhin, Z. Ul'berg, G. Dvornichenko and B. Deryagin, *Bulletin of the Academy of Sciences of the USSR. Division of Chemical Sciences*, 1982, **31**, 1535–1544.
40 J. L. Wilson, S. Shim, Y. E. Yu, A. Gupta and H. A. Stone, *Langmuir*, 2020, **36**, 7014–7020.
41 H. J. Keh, *Current Opinion in Colloid & Interface Science*, 2016, **24**, 13–22.
42 A. Gupta, B. Rallabandi and H. A. Stone, *Physical Review Fluids*, 2019, **4**, 043702.
43 B. M. Alessio, S. Shim, A. Gupta and H. A. Stone, *Journal of Fluid Mechanics*, 2022, **942**, A23.
44 H. J. Keh and S. B. Chen, *Langmuir*, 1993, **9**, 1142–1149.
45 S. Marbach and L. Bocquet, *Chemical Society Reviews*, 2019, **48**, 3102–3144.
46 R. J. Hunter, *Zeta Potential in Colloid Science: Principles and Applications*, Academic Press, 1981.
47 R. F. Probstein, *Physicochemical Hydrodynamics: An Introduction*, John Wiley & Sons, 2nd edn, 1994.
48 J. N. Israelachvili, *Intermolecular and Surface Forces*, Academic Press, 3rd edn, 2011.
49 Á. V. Delgado, F. González-Caballero, R. J. Hunter, L. K. Koopal and J. Lyklema, *Pure and Applied Chemistry*, 2005, **77**, 1753–1805.
50 G. K. Batchelor, *An Introduction to Fluid Dynamics*, Cambridge University Press, 1967.
51 L. G. Leal, *Advanced Transport Phenomena: Fluid Mechanics and Convective Transport Processes*, Cambridge University Press, 2007.
52 J. Happel and H. Brenner, *Low Reynolds Number Hydrodynamics: With Special Applications to Particulate Media*, Springer, 1983.
53 S. Kim and S. J. Karrila, *Microhydrodynamics: Principles and Selected Applications*, Dover Publications, 1991.
54 S. Shin, J. T. Ault, J. Feng, P. B. Warren and H. A. Stone, *Advanced Materials*, 2017, **29**, 1701516.
55 Y. Xia and G. M. Whitesides, *Angewandte Chemie International Edition*, 1998, **37**, 550–575.
56 D. Bartolo, G. Degré, P. Nghe and V. Studer, *Lab on a Chip*, 2008, **8**, 274–279.
57 D. C. Duffy, J. C. McDonald, O. J. A. Schueller and G. M. Whitesides, *Analytical Chemistry*, 1998, **70**, 4974–4984.
58 J. C. McDonald, D. C. Duffy, J. R. Anderson, D. T. Chiu, H. Wu, O. J. A. Schueller and G. M. Whitesides, *Electrophoresis*, 2000, **21**, 27–40.
59 G. M. Whitesides, *Nature*, 2006, **442**, 368–373.
60 C. A. Schneider, W. S. Rasband and K. W. Eliceiri, *Nature Methods*, 2012, **9**, 671–675.
61 E. R. Weeks and J. C. Crocker, *Online resource*, 2012.
62 A. Ozcelik, *Biomimetics*, 2026, **11**, 181.
63 M. S. Khan, R. H. Julio, M. Ali, S. Sachs, C. Cierpka, J. König and J. Park, *Lab on a Chip*, 2026, **26**, 1025–1052.
64 A. D. Stroock, M. Weck, D. T. Chiu, W. T. S. Huck, P. J. A. Kenis, R. F. Ismagilov and G. M. Whitesides, *Physical Review Letters*, 2000, **84**, 3314–3317.
65 A. D. Stroock and G. M. Whitesides, *Accounts of Chemical Research*, 2003, **36**, 597–604.
66 C. Jiang, G. Wang, R. Hein, N. Liu, X. Luo and J. J. Davis, *Chemical Reviews*, 2020, **120**, 3852–3889.
67 P.-H. Lin and B.-R. Li, *Analyst*, 2020, **145**, 1110–1120.
68 S. Szunerits, Q. Pagneux, Y. Ben M'Barek, S. Vassal and R. Boukherroub, *Bioelectrochemistry*, 2023, **153**, 108479.
69 E. Jarosińska, Z. Zambrowska and E. Witkowska Nery, *ACS Omega*, 2024, **9**, 4572–4580.
70 N. Singh, G. T. Vladisavljević, F. Nadal, C. Cottin-Bizonne, C. Pirat and G. Bolognesi, *Physical Review Letters*, 2020, **125**, 248002.
71 N. Singh, G. T. Vladisavljević, F. Nadal, C. Cottin-Bizonne, C. Pirat and G. Bolognesi, *Langmuir*, 2022, **38**, 14053–14062.
72 A. Chakra, N. Singh, G. T. Vladisavljević, F. Nadal, C. Cottin-Bizonne, C. Pirat and G. Bolognesi, *ACS Nano*, 2023, **17**, 14644–14657.
73 M. Howard, B. J. Zern, A. C. Anselmo, V. V. Shuvaev, S. Mitragotri and V. Muzykantov, *ACS Nano*, 2014, **8**, 4100–4132.
74 P. M. Glassman, J. W. Myerson, L. T. Ferguson, R. Y. Kiseleva, V. V. Shuvaev, J. S. Brenner and V. R. Muzykantov, *Advanced Drug Delivery Reviews*, 2020, **157**, 96–117.
75 S. w. Park, J. Lee, H. Yoon and S. Shin, *Energy & Fuels*, 2021, **35**, 4885–4892.
76 I. L. Molnar, E. Pensini, M. A. Asad, C. A. Mitchell, L. C. Nitsche, L. J. Pyrak-Nolte, G. L. Miño and M. M. Krol, *Transport in Porous Media*, 2019, **130**, 129–156.
77 C. T. Nguyen, E.-H. Cho, B. Gu, S. Lee, H.-S. Kim, J. Park, N.-K. Yu, S. Shin, B. Shong, J. Y. Lee and H.-B.-R. Lee, *Nature Communications*, 2022, **13**, 7597.
78 B. J. Kirby and E. F. Hasselbrink, *Electrophoresis*, 2004, **25**, 203–213.

View Article Online
DOI: 10.1039/D6NR00004E

Data availability

The data supporting this article, including the processed datasets, representative raw microscopy images, and analysis scripts, are provided in the Supplementary Information (SI).